

90 to 95% (Fig. 2D). This phenomenon may stem from the insolubility of the organic fluorophore in water and results in efficient aggregate emission with a high f_w . The molecular fluorophore **HLZ-BTED** with efficient aggregate emission in water is eligible for further NIR-II biomedical fluorescence imaging.

To illustrate the feasibility of **HLZ-BTED** for bioimaging application, we fabricated water-soluble and biocompatible AIE dots (**HLZ-BTED** dots) through a nanoprecipitation method by using 1,2-distearoyl-*sn*-glycero-3-phosphoethanolamine-*N*-(methoxy(polyethylene glycol)-5000) (DSPE-PEG₅₀₀₀) as the encapsulation matrix (Fig. 3A). Briefly, a **HLZ-BTED**/THF mixture was quickly added into the DSPE-PEG₅₀₀₀ deionized water solution in an ice bath under continuous sonication. Then, the remaining THF in the mixture was removed completely under a nitrogen flow. The redundant DSPE-PEG₅₀₀₀ was removed by ultrafiltration using 50 kDa centrifugal filter devices to obtain **HLZ-BTED** dots. The synthesized **HLZ-BTED** dots showed high monodispersity and homogeneity with an average particle size of ~ 50 nm as determined by transmission electron microscopy (TEM, Fig. 3B) and a hydrodynamic diameter of ~ 60 nm as determined by dynamic light scattering (DLS, Fig. S3A†). The zeta potential distribution of the **HLZ-BTED** dots was measured and the colloidal stability of the AIE dots under physiological conditions was evaluated. The results have demonstrated that the nanoparticles have negative surface

charges and excellent stability in water and physiological media (Fig. S3B and S4†). The UV-vis-NIR absorption and NIR-II fluorescence emission spectra of the **HLZ-BTED** dots in water were investigated under 785 nm excitation. As shown in Fig. 3C, the absorption peak was at ~ 805 nm, while the fluorescence emission peak was at ~ 1034 nm with a 229 nm Stokes shift. In Fig. S2,† the NIR-II quantum yield (QY) of the **HLZ-BTED** dots in water was measured to be 0.18% under 785 nm laser excitation using IR-26 dye as a reference (QY = 0.5%), which was around two-fold higher than that of the fluorophore in THF (QY = 0.1%) and matched well with the results for exploring the AIE property in Fig. 2D. The large Stokes shift and appropriate fluorescence efficiency of the **HLZ-BTED** dots are remarkably beneficial for NIR-II AIE bioimaging.

The **HLZ-BTED** dots showed superior photostability in water, phosphate buffered saline (PBS), and fetal bovine serum (FBS) under continuous 808 nm laser irradiation for 1 h at a power density of 180 mW cm^{-2} , while indocyanine green (ICG), which is approved by the FDA for NIR-I biomedical fluorescence imaging in water, showed a drastic decrease in fluorescence intensity using the same measurement method (Fig. 3D). To explore time-dependent fluorescence stability in different media, the variation in fluorescence intensity of the **HLZ-BTED** dots in water, PBS, and FBS was observed at different time points (2 min, 60 min and 30 h) after incubation at room temperature, exhibiting excellent temporal stability without an obvious change in the FL intensity (Fig. 3E). These photo and temporal stability results demonstrated that the **HLZ-BTED** dots could be useful for long-term *in vivo* imaging.

To further demonstrate the capability of the **HLZ-BTED** dots as a NIR-II imaging contrast agent *in vivo*, the pharmacokinetics and potential toxicity of the **HLZ-BTED** dots were carefully evaluated. The pharmacokinetics were studied *via* the measurement of the blood circulation half-life. The half-life time of the **HLZ-BTED** dots was 204 min (Fig. S5†). The long circulation time of the AIE dots in blood was mainly due to the strong interaction between the **HLZ-BTED** dots and serum albumin (Fig. S6,† $K_D = 0.0303 \text{ nM}$), and allowed them to reach their imaging target. The cytotoxicity of the **HLZ-BTED** dots to 4T1 mammary cancer and L929 mouse fibroblast cell lines was demonstrated using the standard 3-(4,5-dimethylthiazol-2-yl)-2,5-diphenyl tetrazolium bromide (MTT) assay. As shown in Fig. 4A, no obvious cytotoxicity was observed even when the concentration was increased to $150 \mu\text{g mL}^{-1}$. The long-term potential toxicity of the **HLZ-BTED** dots in normal KM mice was evaluated. A solution of PBS (0.2 mL, $n = 3$) and medium dose **HLZ-BTED** dots (0.2 mL, 7.5 mg kg^{-1} , $n = 3$), or high dose **HLZ-BTED** dots (0.2 mL, 15 mg kg^{-1} , $n = 3$) was injected into normal KM mice by intravenous injection (i.v.) *via* the tail vein. No significant difference in body weight was observed between the PBS control group and the **HLZ-BTED** dot administered groups during the research process (31 days) (Fig. 4B). Moreover, the major organs of the mice, including the heart, liver, spleen, lungs and kidneys were obtained and stained with hematoxylin and eosin (H&E) for histopathological study at 31 days after treatment. The H&E staining results shown in Fig. 4C exhibited no obvious necrosis or inflammation lesions in all the major



Fig. 3 (A) Schematic illustration of the preparation method of NIR-II AIE nanoparticles (**HLZ-BTED** dots) *via* micellization. (B) Representative TEM image of the **HLZ-BTED** dots. Scale bar: 100 nm. (C) UV-vis-NIR absorption spectrum and NIR-II fluorescence emission spectrum (785 nm laser excitation) of the **HLZ-BTED** dots in aqueous solution. (D) Photo-stability test of the AIE **HLZ-BTED** dots in water, PBS, fetal bovine serum (FBS) and ICG in water under continuous 808 nm laser (180 mW cm^{-2}) irradiation for 60 min. (E) Quantitative analysis of the NIR-II fluorescence intensity of the **HLZ-BTED** dots in water, PBS, and FBS after 2 min to 30 h incubation.



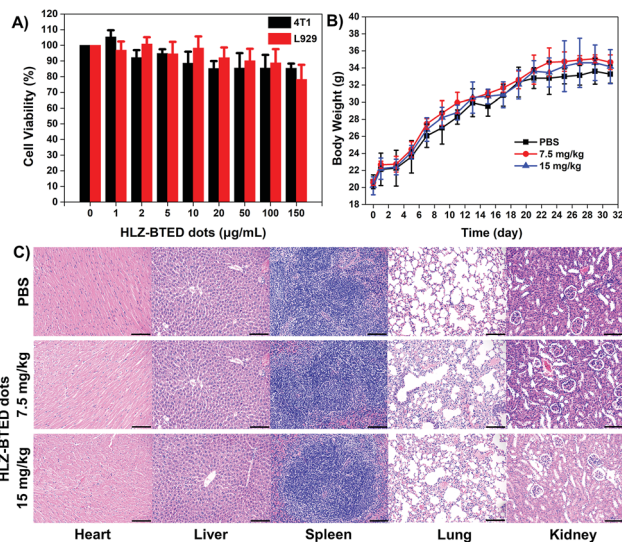


Fig. 4 Biocompatibility study of the HLZ-BTED dots. (A) Cell viability of 4T1 and L929 cells after incubation with different concentrations of the HLZ-BTED dots for 24 h ($n = 3$). (B) Body weight of normal mice on different days ($n = 3$) treated with PBS, 7.5 mg kg^{-1} , and 15 mg kg^{-1} HLZ-BTED dots. (C) Representative hematoxylin and eosin stained images of major organs (heart, liver, spleen, lungs, and kidneys) from the control mice and HLZ-BTED dot injected mice at 31 days post-treatment. Scale bar: $100 \mu\text{m}$.

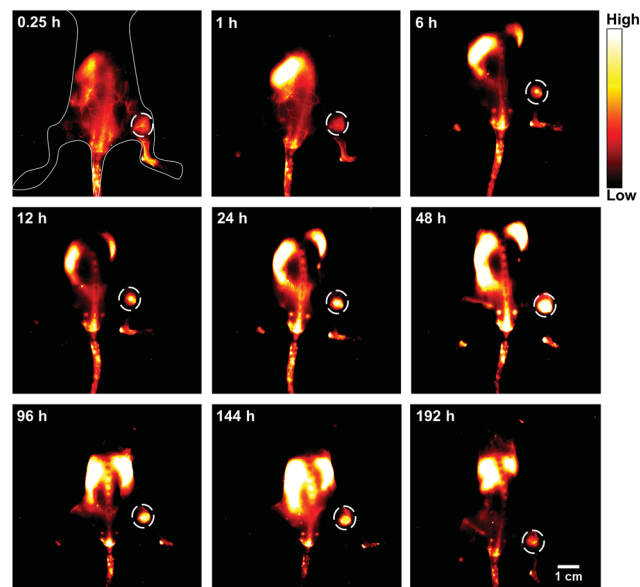


Fig. 5 Representative *in vivo* long-term NIR-II fluorescence images (808 nm excitation, 90 mW cm^{-2} , 1000 nm LP , 100 ms , $n = 3$) of the 4T1 breast tumor model at different time points after tail vein injection of the HLZ-BTED dots (0.2 mL , 10 mg kg^{-1}). The white circles indicate the location of the 4T1 tumor. Scale bar: 1 cm .

organs, indicating that the HLZ-BTED dots have excellent biocompatibility and are more applicable for NIR-II bioimaging *in vivo*.

Breast cancer is the most common cancer in women worldwide.¹⁹ Early diagnosis of breast cancer with the use of systemic therapy has an excellent prognosis and increases the long-term disease-free survival (DFS).²⁰ Firstly, the *in vitro* cellular endocytosis of the HLZ-BTED dots was studied using 4T1 breast cancer cells. As shown in Fig. S7,† the NIR-II fluorescence intensity of the 4T1 cells incubated with the HLZ-BTED dots showed explicit time dependence, suggesting that the AIE dots can permeate into the cells *via* the cellular membrane. To explore the ability of the HLZ-BTED dots to diagnose breast cancer early, a mouse model of breast cancer was established. 4T1 breast cancer cells (roughly 2×10^6) were subcutaneously injected into the right leg of female BALB/c mice. NIR-II fluorescence imaging of 4T1 breast tumors was carried out by intravenously injecting the AIE dots (0.2 mL , 10 mg kg^{-1}) into 4T1 tumor-bearing mice ($n = 3$) through the tail vein when the tumors reached $\sim 60 \text{ mm}^3$ in a week. The fluorescence intensity (1000 nm LP , 100 ms) in tumors reached the highest level at 48 h post-injection under 808 nm excitation with a power density of 90 mW cm^{-2} (Fig. 5 and S8†). For up to 8 days post-injection, the NIR-II fluorescence signal of tumors was extremely strong and clearly delineated the normal tissues, indicating that the AIE HLZ-BTED dots are adequate for long-term tumor imaging and real-time image-based monitoring for solid tumor therapy. An *ex vivo* biodistribution study was performed for the HLZ-BTED dots to evaluate their distribution in major organs at 192 h (Fig. S9†). High accumulation was observed in the liver

and spleen, which suggested that the clearance routes of the HLZ-BTED dots were through the hepatobiliary system. In addition, the AIE dots showed high accumulation in 4T1 tumors for up to 8 days (Fig. S9†).

Transcatheter arterial embolization (TAE) is widely used in the clinic to increase survival for cancer patients who are not suitable for chemotherapy and surgical resection.²¹ To estimate the potential feasibility of the HLZ-BTED dots as a NIR-II contrast agent for the *in vivo* imaging of the tumor-feeding blood vessels to implement TAE, the AIE HLZ-BTED dots were *i.v.* injected into 4T1 tumor bearing BALB/c mice ($n = 3$). At 2 min post-injection, the tumor vasculature was visualized using an InGaAs camera with 1000 nm (Fig. 6A, 200 ms exposure time) and 1250 nm (Fig. 6B, 800 ms exposure time) long-pass filters under 808 nm laser excitation. The NIR-II fluorescence images of the 4T1 tumor blood vessels showed a more distinct vascular network with the 1250 nm long-pass filter than with the 1000 nm one, owing to both reduced biological auto-fluorescence and photon scattering in the longer wavelength NIR-II region. Meanwhile a similar image quality *via* different long-pass filters has been demonstrated in the hind limb vasculature of C57BL/6 mice (Fig. 6C and D). Moreover, we performed a surgery to induce incomplete hind limb ischemia to mimic the NIR-II fluorescence imaging-guided vascular embolization procedure. The occlusion site of the blood supply vessels was precisely monitored by NIR-II imaging using the HLZ-BTED dots (Fig. 6E). Then the capability of long-term vasculature imaging using the HLZ-BTED dots was investigated. As shown in Fig. 6F, at 4 h post-injection, the vasculature was still clearly visualized through NIR-II imaging which would be adequate for surgical operation. The resolution ($497.6 \mu\text{m}$) of the hind limb



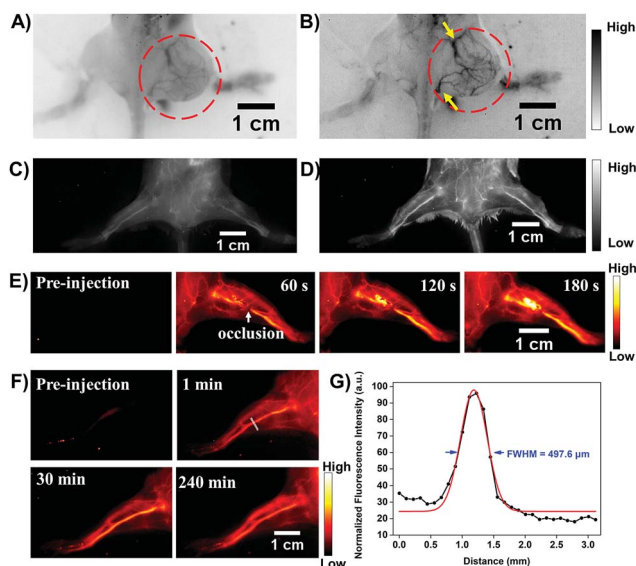


Fig. 6 (A and B) *In vivo* visualization of tumor-feeding vessels. NIR-II tumor blood vessel fluorescence images of the 4T1 breast tumor-bearing mice were obtained at 2 min post tail vein injection of the HLZ-BTED dots (0.2 mL, 10 mg kg⁻¹) with 1000 nm (A), 200 ms, 808 nm excitation, 90 mW cm⁻² and 1250 nm (B), 800 ms, 808 nm excitation, 180 mW cm⁻² long-pass filters, respectively. The red circles indicate the location of the tumor, and yellow arrows indicate the tumor-feeding arteries. (C and D) NIR-II fluorescence images of the hind limb vessels in C57BL/6 mice at 2 min after tail vein injection of the HLZ-BTED dots (0.2 mL, 15 mg kg⁻¹) with 1000 nm (C), 60 ms, 808 nm excitation, 90 mW cm⁻² and 1250 nm (D), 500 ms, 808 nm excitation, 180 mW cm⁻² long-pass filters, respectively. (E) *In vivo* NIR-II fluorescence images (1250 nm LP, 400 ms, 808 nm excitation, 180 mW cm⁻²) of incomplete left hind limb ischemia pre-injection and 60 s, 120 s, and 180 s after HLZ-BTED dot injection, where the white arrow located the occlusion site in the femoral artery. (F) Intravital long-term hind limb vasculature NIR-II imaging (1250 nm LP, 400 ms, 808 nm excitation, 180 mW cm⁻²) from 0 min to 240 min after tail vein injection of the HLZ-BTED dots. Scale bar (A–F): 1 cm. (G) The vessel FWHM width based on the cross-sectional intensity profile measured along the white line in (F) (1 min) with the peak fitted to Gaussian functions (the red curve is the Gaussian fit to the profile).

vasculature was investigated *via* the Gaussian-fitted full width at half maximum (FWHM), which further confirmed the excellent ability of the HLZ-BTED dots to precisely map vascular vessels with NIR-II imaging (Fig. 6G).

The gastrointestinal (GI) tract is an organ system, which includes all organ structures between the mouth and the anus, such as the esophagus, stomach, small intestine, and large intestine. The GI tract is responsible for ingesting and digesting food, extracting and absorbing nutrients, and expelling the waste as feces. Recently, non-invasive imaging modalities such as positron emission tomography (PET),²² magnetic resonance imaging (MRI),²³ X-ray computed tomography (CT),²⁴ and photoacoustic (PA)²² imaging, have played an important role in GI function research and the diagnosis and prognosis of GI diseases. However, these imaging modalities are limited by their serious drawbacks, notably radiation risk, expensive instrument cost, long imaging times and limited spatial resolution for real-time gut function study such as physiological or

pathological intestinal motility. NIR-II fluorescence imaging may provide a reliable method for monitoring intestinal motility disorders or dysfunction and providing evaluation information of GI therapeutic agents *in vivo* due to superior temporal-spatial resolution.²⁵ Therefore, as a proof of concept, we demonstrated the feasibility of the AIE HLZ-BTED dots for *in vivo* NIR-II imaging of the GI tract by oral administration. First, the fluorescence intensity and hydrodynamic sizes of the HLZ-BTED dots in different pH buffers ranging from 1 to 9 or in gastric pH 1 buffer were investigated respectively. No significant difference was observed between different conditions, demonstrating the excellent stability and capability of the AIE dots as a GI tract contrast agent (Fig. S10†). Second, healthy BALB/c mice ($n = 3$) were gavaged with the HLZ-BTED dots (0.1 mL, 5 mg kg⁻¹) for real-time imaging of intestinal motility and monitoring the behavior of micelles within the GI tract. NIR-II fluorescence images at different time points (5, 10, 20, 30, 60, 90, 180, 480, 600 and 1440 min) were obtained under 808 nm laser irradiation (180 mW cm⁻², within the safety limits (329 mW cm⁻²) determined by the International Commission on Non-ionizing Radiation Protection) through an InGaAs camera (200 ms exposure time) with a 1250 nm long-pass filter. As shown in Fig. 7A, from 5 min to 480 min after gavaging, the fluorescent signals were observed in the stomach, duodenum, jejunum, ileum, cecum, and colon. During the imaging procedure of the intestine, the contractile function of the intestine was demonstrated by the recorded Movie S1.† The fluorescence intensity movement in the small intestine indicated vigorous



Fig. 7 (A and B) Representative non-invasive NIR-II fluorescence images (1250 nm LP, 200 ms, 808 nm excitation, 180 mW cm⁻²) of the gastrointestinal tract (GI tract) in BALB/c mice gavaged with the HLZ-BTED dots (0.1 mL, 5 mg kg⁻¹) for real-time monitoring of gastrointestinal peristalsis of normal mice (A) and mice anesthetized (B) using pentobarbital sodium ($n = 3$ mice). The white arrow indicates the feces of mice (Fig. 7A, 600 min). Scale bar: 1 cm.



- Y. Zhong, J. Su, A. L. Antaris, Y. Xia, J. Luo, Y. Liang and H. Dai, *Nat. Commun.*, 2018, **9**, 1171.
- 2 (a) E. C. Rossi, A. Ivanova and J. F. Boggess, *Gynecol. Oncol.*, 2012, **124**, 78–82; (b) G. Wishart, S.-W. Loh, L. Jones and J. Benson, *Eur. J. Surg. Oncol.*, 2012, **38**, 651–656; (c) C. Hirche, D. Murawa, Z. Mohr, S. Kneif and M. Hünerbein, *Breast Cancer Res. Treat.*, 2010, **121**, 373–378.
- 3 (a) M. Herranz and A. Ruibal, *J. Oncol.*, 2012, **2012**, 863747; (b) C. Zeng, W. Shang, X. Liang, X. Liang, Q. Chen, C. Chi, Y. Du, C. Fang and J. Tian, *ACS Appl. Mater. Interfaces*, 2016, **8**, 29232–29241; (c) S. Luo, E. Zhang, Y. Su, T. Cheng and C. Shi, *Biomaterials*, 2011, **32**, 7127–7138; (d) J. Yang, Q. Xie, H. Zhou, L. Chang, W. Wei, Y. Wang, H. Li, Z. Deng, Y. Xiao, J. Wu, P. Xu and X. Hong, *J. Proteome Res.*, 2018, **17**, 2428–2439.
- 4 (a) Y. Sun, X. Zeng, Y. Xiao, C. Liu, H. Zhu, H. Zhou, Z. Chen, F. Xu, J. Wang, M. Zhu, J. Wu, M. Tian, H. Zhang, Z. Deng, Z. Cheng and X. Hong, *Chem. Sci.*, 2018, **9**, 2092–2097; (b) Y. Sun, M. Ding, X. Zeng, Y. Xiao, H. Wu, H. Zhou, B. Ding, C. Qu, W. Hou, A. Erbu, Y. Zhang, Z. Cheng and X. Hong, *Chem. Sci.*, 2017, **8**, 3489–3493.
- 5 (a) F. Ding, Y. Zhan, X. Lu and Y. Sun, *Chem. Sci.*, 2018, **9**, 4370–4380; (b) G. Hong, A. L. Antaris and H. Dai, *Nat. Biomed. Eng.*, 2017, **1**, 0010; (c) F. Ding, S. Chen, W. Zhang, Y. Tu and Y. Sun, *Bioorg. Med. Chem.*, 2017, **25**, 5179–5184; (d) Y. Xu, M. Tian, H. Zhang, Y. Xiao, X. Hong and Y. Sun, *Chin. Chem. Lett.*, 2018, **29**, 1093–1097; (e) S. He, J. Song, J. Qu and Z. Cheng, *Chem. Soc. Rev.*, 2018, **47**, 4258–4278; (f) W. Zhu, *Sci. China: Chem.*, 2016, **59**, 203–204; (g) B. Li, L. Lu, M. Zhao, Z. Lei and F. Zhang, *Angew. Chem., Int. Ed.*, 2018, **57**, 7483–7487; (h) H. Zhou, Y. Xiao and X. Hong, *Chin. Chem. Lett.*, 2018, **29**, 1425–1428; (i) J. Yang and X. Hong, *Sci. China: Chem.*, 2018, DOI: 10.1007/s11426-018-9341-7.
- 6 (a) L. Liu, S. Wang, B. Zhao, P. Pei, Y. Fan, X. Li and F. Zhang, *Angew. Chem.*, 2018, **130**, 7640–7644; (b) Y. Fan, P. Wang, Y. Lu, R. Wang, L. Zhou, X. Zheng, X. Li, J. A. Piper and F. Zhang, *Nat. Nanotechnol.*, 2018, **13**, 941–946; (c) P. Wang, Y. Fan, L. Lu, L. Liu, L. Fan, M. Zhao, Y. Xie, C. Xu and F. Zhang, *Nat. Commun.*, 2018, **9**, 2898; (d) Y. Zhong, Z. Ma, S. Zhu, J. Yue, M. Zhang, A. L. Antaris, J. Yuan, R. Cui, H. Wan, Y. Zhou, W. Wang, N. F. Huang, J. Luo, Z. Hu and H. Dai, *Nat. Commun.*, 2017, **8**, 737; (e) X. Jiang, C. Cao, W. Feng and F. Li, *J. Mater. Chem. B*, 2016, **4**, 87–95; (f) D. Naczynski, M. Tan, M. Zevon, B. Wall, J. Kohl, A. Kulesa, S. Chen, C. Roth, R. Riman and P. Moghe, *Nat. Commun.*, 2013, **4**, 2199.
- 7 (a) M. Zhang, J. Yue, R. Cui, Z. Ma, H. Wan, F. Wang, S. Zhu, Y. Zhou, Y. Kuang, Y. Zhong, D.-W. Pang and H. Dai, *Proc. Natl. Acad. Sci. U. S. A.*, 2018, 201806153; (b) Z. Ma, M. Zhang, J. Yue, C. Alcazar, Y. Zhong, T. C. Doyle, H. Dai and N. F. Huang, *Adv. Funct. Mater.*, 2018, **28**, 1803417; (c) G. Chen, S. Lin, D. Huang, Y. Zhang, C. Li, M. Wang and Q. Wang, *Small*, 2018, **14**, 1702679; (d) C. Li, Y. Zhang, G. Chen, F. Hu, K. Zhao and Q. Wang, *Adv. Mater.*, 2017, **29**, 1605754; (e) G. Chen, F. Tian, C. Li, Y. Zhang, Z. Weng, Y. Zhang, R. Peng and Q. Wang, *Biomaterials*, 2015, **53**, 265–273; (f) G. Hong, J. T. Robinson, Y. Zhang, S. Diao, A. L. Antaris, Q. Wang and H. Dai, *Angew. Chem., Int. Ed.*, 2012, **51**, 9818–9821; (g) Y. Zhang, G. Hong, Y. Zhang, G. Chen, F. Li, H. Dai and Q. Wang, *ACS Nano*, 2012, **6**, 3695–3702.
- 8 (a) G. Hong, S. Diao, J. Chang, A. L. Antaris, C. Chen, Z. Bo, Z. Su, D. N. Atochin, P. L. Huang, K. I. Andreasson, C. J. Kuo and H. Dai, *Nat. Photonics*, 2014, **8**, 723–730; (b) J. T. Robinson, K. Welscher, S. M. Tabakman, S. P. Sherlock, H. Wang, R. Luong and H. Dai, *Nano Res.*, 2010, **3**, 779–793.
- 9 (a) K. Shou, Y. Tang, H. Chen, S. Chen, L. Zhang, A. Zhang, Q. Fan, A. Yu and Z. Cheng, *Chem. Sci.*, 2018, **9**, 3105–3110; (b) G. Hong, Y. Zou, A. L. Antaris, S. Diao, D. Wu, K. Cheng, X. Zhang, C. Chen, B. Liu, Y. He, J. Z. Wu, J. Yuan, B. Zhang, Z. Tao, C. Fukunaga and H. Dai, *Nat. Commun.*, 2014, **5**, 4206.
- 10 (a) A. L. Antaris, H. Chen, K. Cheng, Y. Sun, G. Hong, C. Qu, S. Diao, Z. Deng, X. Hu, B. Zhang, X. Zhang, O. K. Yaghi, Z. R. Alamparambil, X. Hong, Z. Cheng and H. Dai, *Nat. Mater.*, 2016, **15**, 235–242; (b) A. L. Antaris, H. Chen, S. Diao, Z. Ma, Z. Zhang, S. Zhu, J. Wang, A. X. Lozano, Q. Fan, L. Chew, M. Zhu, K. Cheng, X. Hong, H. Dai and Z. Cheng, *Nat. Commun.*, 2017, **8**, 15269; (c) Y. Feng, S. Zhu, A. L. Antaris, H. Chen, Y. Xiao, X. Lu, L. Jiang, S. Diao, K. Yu, Y. Wang, S. Herraiz, J. Yue, X. Hong, G. Hong, Z. Cheng, H. Dai and A. J. Hsueh, *Chem. Sci.*, 2017, **8**, 3703–3711.
- 11 (a) K. Shou, C. Qu, Y. Sun, H. Chen, S. Chen, L. Zhang, H. Xu, X. Hong, A. Yu and Z. Cheng, *Adv. Funct. Mater.*, 2017, **27**, 1700995; (b) S. Zhu, Q. Yang, A. L. Antaris, J. Yue, Z. Ma, H. Wang, W. Huang, H. Wan, J. Wang, S. Diao, B. Zhang, X. Li, Y. Zhong, K. Yu, G. Hong, J. Luo, Y. Liang and H. Dai, *Proc. Natl. Acad. Sci. U. S. A.*, 2017, **114**, 962–967; (c) Q. Yang, Z. Ma, H. Wang, B. Zhou, S. Zhu, Y. Zhong, J. Wang, W. Hao, A. Antaris, M. Rui, X. Zhang, J. Yang, X. Zhang, H. Sun, W. Liu, Y. Liang and H. Dai, *Adv. Mater.*, 2017, **29**, 1605497; (d) Y. Sun, C. Qu, H. Chen, M. He, C. Tang, K. Shou, S. Hong, M. Yang, Y. Jiang, B. Ding, Y. Xiao, L. Xing, X. Hong and Z. Cheng, *Chem. Sci.*, 2016, **7**, 6203–6207; (e) Q. Yang, Z. Hu, S. Zhu, R. Ma, H. Ma, Z. Ma, H. Wan, T. Zhu, Z. Jiang, W. Liu, L. Jiao, H. Sun, Y. Liang and H. Dai, *J. Am. Chem. Soc.*, 2018, **140**, 1715–1724; (f) S. Zhu, S. Herraiz, J. Yue, M. Zhang, H. Wan, Q. Yang, Z. Ma, Y. Wang, J. He, A. L. Antaris, Y. Zhong, S. Diao, Y. Feng, Y. Zhou, K. Yu, G. Hong, Y. Liang, A. J. Hsueh and H. Dai, *Adv. Mater.*, 2018, **30**, 1705799.
- 12 J. Luo, Z. Xie, J. W. Lam, L. Cheng, H. Chen, C. Qiu, H. S. Kwok, X. Zhan, Y. Liu, D. Zhu and B. Z. Tang, *Chem. Commun.*, 2001, 1740–1741.
- 13 (a) Z. Chen, J. Zhang, M. Song, J. Yin, G.-A. Yu and S. H. Liu, *Chem. Commun.*, 2015, **51**, 326–329; (b) J. Mei, N. L. Leung, R. T. Kwok, J. W. Lam and B. Z. Tang, *Chem. Rev.*, 2015, **115**, 11718–11940; (c) G. Feng and B. Liu, *Acc. Chem. Res.*, 2018, **51**, 1404–1414; (d) J. Shi, Q. Deng, C. Wan, M. Zheng, F. Huang and B. Tang, *Chem. Sci.*, 2017, **8**, 6188–6195; (e) T. He, N. Niu, Z. Chen, S. Li, S. Liu and J. Li, *Adv. Funct. Mater.*, 2018, **28**, 1706196; (f) Q. Hu, M. Gao, G. Feng and



